Biomedical Optics EXPRESS

Fast 3D visualization of endogenous brain signals with high-sensitivity laser scanning photothermal microscopy

Jun Miyazaki,[1,2,*] Tadatsune Iida,[3] Shinji Tanaka,[3] Akiko Hayashi-Takagi,[4] Haruo Kasai,[2,4] Shigeo Okabe[3] and Takayoshi Kobayashi[1,2,5,6]

[1]*Advanced Ultrafast Laser Research Center, The University of Electro-Communications, 1-5-1 Chofugaoka, Chofu, Tokyo, 182-8585, Japan*
[2]*JST, CREST, K' Gobancho, 7, Gobancho, Chiyoda-ku, Tokyo 102-0076, Japan*
[3]*Department of Cellular Neurobiology, Graduate School of Medicine, The University of Tokyo, 7-3-1, Hongo, Bunkyoku, Tokyo, 113-0033, Japan*
[4]*Department of Structural Physiology, Graduate School of Medicine, The University of Tokyo, 7-3-1, Hongo, Bunkyoku, Tokyo, 113-0033, Japan*
[5]*Department of Electrophysics, National Chiao-Tung University, Hsinchu 300, Taiwan*
[6]*Institute of Laser Engineering, Osaka University, 2-6 Yamada-oka, Suita, Osaka 565-0971, Japan*
[*]*miyazaki@ils.uec.ac.jp*

Abstract: A fast, high-sensitivity photothermal microscope was developed by implementing a spatially segmented balanced detection scheme into a laser scanning microscope. We confirmed a 4.9 times improvement in signal-to-noise ratio in the spatially segmented balanced detection compared with that of conventional detection. The system demonstrated simultaneous bi-modal photothermal and confocal fluorescence imaging of transgenic mouse brain tissue with a pixel dwell time of 20 μs. The fluorescence image visualized neurons expressing yellow fluorescence proteins, while the photothermal signal detected endogenous chromophores in the mouse brain, allowing 3D visualization of the distribution of various features such as blood cells and fine structures probably due to lipids. This imaging modality was constructed using compact and cost-effective laser diodes, and will thus be widely useful in the life and medical sciences.

OCIS codes: (170.6900) Three-dimensional microscopy; (350.5340) Photothermal effects.

References and links

1. E. Tamaki, K. Sato, M. Tokeshi, K. Sato, M. Aihara, and T. Kitamori, "Single-cell analysis by a scanning thermal lens microscope with a microchip: direct monitoring of cytochrome c distribution during apoptosis process," Anal. Chem. **74**(7), 1560–1564 (2002).
2. D. A. Nedosekin, E. I. Galanzha, S. Ayyadevara, R. J. Shmookler Reis, and V. P. Zharov, "Photothermal confocal spectromicroscopy of multiple cellular chromophores and fluorophores," Biophys. J. **102**(3), 672–681 (2012).
3. A. V. Brusnichkin, D. A. Nedosekin, E. I. Galanzha, Y. A. Vladimirov, E. F. Shevtsova, M. A. Proskurnin, and V. P. Zharov, "Ultrasensitive label-free photothermal imaging, spectral identification, and quantification of cytochrome c in mitochondria, live cells, and solutions," J. Biophotonics **3**(12), 791–806 (2010).
4. S. Lu, W. Min, S. Chong, G. R. Holtom, and X. S. Xie, "Label-free imaging of heme proteins with two-photon excited photothermal lens microscopy," Appl. Phys. Lett. **96**(11), 113701 (2010).
5. J. Miyazaki, H. Tsurui, K. Kawasumi, and T. Kobayashi, "Simultaneous dual-wavelength imaging of nonfluorescent tissues with 3D subdiffraction photothermal microscopy," Opt. Express **23**(3), 3647–3656 (2015).
6. C. Leduc, S. Si, J. Gautier, M. Soto-Ribeiro, B. Wehrle-Haller, A. Gautreau, G. Giannone, L. Cognet, and B. Lounis, "A highly specific gold nanoprobe for live-cell single-molecule imaging," Nano Lett. **13**(4), 1489–1494 (2013).
7. C. Leduc, J. M. Jung, R. P. Carney, F. Stellacci, and B. Lounis, "Direct investigation of intracellular presence of gold nanoparticles via photothermal heterodyne imaging," ACS Nano **5**(4), 2587–2592 (2011).
8. L. Cognet, C. Tardin, D. Boyer, D. Choquet, P. Tamarat, and B. Lounis, "Single metallic nanoparticle imaging for protein detection in cells," Proc. Natl. Acad. Sci. U.S.A. **100**(20), 11350–11355 (2003).
9. J. Miyazaki, H. Tsurui, and T. Kobayashi, "Reduction of distortion in photothermal microscopy and its application to the high-resolution three-dimensional imaging of nonfluorescent tissues," Biomed. Opt. Express **6**(9), 3217–3224 (2015).

#259725 Received 19 Feb 2016; revised 24 Mar 2016; accepted 25 Mar 2016; published 5 Apr 2016

10. A. P. Jathoul, J. Laufer, O. Ogunlade, B. Treeby, B. Cox, E. Zhang, P. Johnson, A. R. Pizzey, B. Philip, T. Marafioti, M. F. Lythgoe, R. B. Pedley, M. A. Pule, and P. Beard, "Deep in vivo photoacoustic imaging of mammalian tissues using a tyrosinase-based genetic reporter," Nat. Photonics **9**, 239–246 (2015).
11. J. Yao, L. Wang, J. M. Yang, K. I. Maslov, T. T. Wong, L. Li, C. H. Huang, J. Zou, and L. V. Wang, "High-speed label-free functional photoacoustic microscopy of mouse brain in action," Nat. Methods **12**(5), 407–410 (2015).
12. C. Pache, N. L. Bocchio, A. Bouwens, M. Villiger, C. Berclaz, J. Goulley, M. I. Gibson, C. Santschi, and T. Lasser, "Fast three-dimensional imaging of gold nanoparticles in living cells with photothermal optical lock-in Optical Coherence Microscopy," Opt. Express **20**(19), 21385–21399 (2012).
13. J. M. Tucker-Schwartz, T. A. Meyer, C. A. Patil, C. L. Duvall, and M. C. Skala, "In vivo photothermal optical coherence tomography of gold nanorod contrast agents," Biomed. Opt. Express **3**(11), 2881–2895 (2012).
14. S. Arunkarthick, M. M. Bijeesh, G. K. Varier, M. Kowshik, and P. Nandakumar, "Laser scanning photothermal microscopy: fast detection and imaging of gold nanoparticles," J. Microsc. **256**(2), 111–116 (2014).
15. W.-S. Chang and S. Link, "Enhancing the sensitivity of single-particle photothermal imaging with thermotropic liquid crystals," J. Phys. Chem. Lett. **3**(10), 1393–1399 (2012).
16. A. N. G. Parra-Vasquez, L. Oudjedi, L. Cognet, and B. Lounis, "Nanoscale Thermotropic Phase Transitions Enhancing Photothermal Microscopy Signals," J. Phys. Chem. Lett. **3**(10), 1400–1403 (2012).
17. J. Miyazaki, H. Tsurui, K. Kawasumi, and T. Kobayashi, "Sensitivity enhancement of photothermal microscopy with radially segmented balanced detection," Opt. Lett. **40**(4), 479–482 (2015).
18. S. Berciaud, D. Lasne, G. A. Blab, L. Cognet, and B. Lounis, "Photothermal heterodyne imaging of individual metallic nanoparticles: Theory versus experiment," Phys. Rev. B **73**(4), 045424 (2006).
19. P. Vermeulen, L. Cognet, and B. Lounis, "Photothermal microscopy: optical detection of small absorbers in scattering environments," J. Microsc. **254**(3), 115–121 (2014).
20. D. Boyer, P. Tamarat, A. Maali, B. Lounis, and M. Orrit, "Photothermal imaging of nanometer-sized metal particles among scatterers," Science **297**(5584), 1160–1163 (2002).
21. A. C. Kwan, K. Duff, G. K. Gouras, and W. W. Webb, "Optical visualization of Alzheimer's pathology via multiphoton-excited intrinsic fluorescence and second harmonic generation," Opt. Express **17**(5), 3679–3689 (2009).
22. C. Krafft, M. Kirsch, C. Beleites, G. Schackert, and R. Salzer, "Methodology for fiber-optic Raman mapping and FTIR imaging of metastases in mouse brains," Anal. Bioanal. Chem. **389**(4), 1133–1142 (2007).
23. C. Krafft, "Bioanalytical applications of Raman spectroscopy," Anal. Bioanal. Chem. **378**(1), 60–62 (2004).
24. N. Benseny-Cases, O. Klementieva, M. Cotte, I. Ferrer, and J. Cladera, "Microspectroscopy (μFTIR) Reveals Co-localization of Lipid Oxidation and Amyloid Plaques in Human Alzheimer Disease Brains," Anal. Chem. **86**(24), 12047–12054 (2014).
25. D. A. Dombeck, K. A. Kasischke, H. D. Vishwasrao, M. Ingelsson, B. T. Hyman, and W. W. Webb, "Uniform polarity microtubule assemblies imaged in native brain tissue by second-harmonic generation microscopy," Proc. Natl. Acad. Sci. U.S.A. **100**(12), 7081–7086 (2003).
26. S. Witte, A. Negrean, J. C. Lodder, C. P. de Kock, G. Testa Silva, H. D. Mansvelder, and M. Louise Groot, "Label-free live brain imaging and targeted patching with third-harmonic generation microscopy," Proc. Natl. Acad. Sci. U.S.A. **108**(15), 5970–5975 (2011).
27. C. L. Evans, X. Xu, S. Kesari, X. S. Xie, S. T. Wong, and G. S. Young, "Chemically-selective imaging of brain structures with CARS microscopy," Opt. Express **15**(19), 12076–12087 (2007).
28. C. W. Freudiger, W. Min, B. G. Saar, S. Lu, G. R. Holtom, C. He, J. C. Tsai, J. X. Kang, and X. S. Xie, "Label-free biomedical imaging with high sensitivity by stimulated Raman scattering microscopy," Science **322**(5909), 1857–1861 (2008).
29. B. R. Hammond, Jr. and L. M. Renzi, "Carotenoids," Adv. Nutr. **4**(4), 474–476 (2013).
30. E. J. Johnson, "A possible role for lutein and zeaxanthin in cognitive function in the elderly," Am. J. Clin. Nutr. **96**(5), 1161S–1165S (2012).
31. F. J. van der Meer, D. J. Faber, I. Cilesiz, M. J. van Gemert, and T. G. van Leeuwen, "Temperature-dependent optical properties of individual vascular wall components measured by optical coherence tomography," J. Biomed. Opt. **11**(4), 041120 (2006).
32. D. Lasne, G. A. Blab, F. De Giorgi, F. Ichas, B. Lounis, and L. Cognet, "Label-free optical imaging of mitochondria in live cells," Opt. Express **15**(21), 14184–14193 (2007).
33. J. P. Liu, Y. Tang, S. Zhou, B. H. Toh, C. McLean, and H. Li, "Cholesterol involvement in the pathogenesis of neurodegenerative diseases," Mol. Cell. Neurosci. **43**(1), 33–42 (2010).

1. Introduction

Photothermal (PT) microscopy can visualize non-fluorescent chromophores with high sensitivity and high spatial resolution. Thus far, it has been applied to visualize the distribution of endogenous chromoproteins in biological specimens such as cytochromes in mitochondria [1–3], hemoglobin in blood vessels [4], and melanin pigments in skin cancer [5]. Furthermore, gold nanoparticles have been used to identify biomolecules in antibody labelling techniques applied in cellular imaging [6–8]. As gold nanoparticles are physiologically inert and do not suffer from photobleaching or photoblinking, they are highly useful in live cell imaging.

#259725 Received 19 Feb 2016; revised 24 Mar 2016; accepted 25 Mar 2016; published 5 Apr 2016

In PT imaging, a sample or a focused laser beam is scanned sequentially point-by-point and the pixel information is assembled into an image. Previously, PT imaging typically used a piezo stage to scan a sample, but stage scanning requires a longer time with integration times per pixel ranging from 1 to 10 ms. In this case, the acquisition time of an image was 4 to 40 minutes for 500 x 500 pixels. One of the advantages of PT microscopy is its 3D imaging capability like confocal microscopy [2, 9]; however, it takes too long to acquire a stack of images at different focal plane depths (a volume scan) using a stage scanning PT microscope. Photoacoustic microscopy (PAM) [10, 11] and PT optical coherent tomography (PTOCT) [12, 13] are powerful techniques for the 3D imaging of optical absorbers *in vivo*, but spatial resolution in PT microscopy is usually better than that of PAM and PTOCT by an order of magnitude. Besides 3D imaging, PT imaging at fast time scales has potential applications for live cell imaging and the tracking of biomolecular transport. PT microscopy equipped with a scanning mirror is a straightforward approach for fast imaging and there have been several reports of laser scanning PT microscopy [4, 14], which allows image acquisition with an 80 μs pixel dwell time so that 500 x 500 pixel images are acquired in 20 s.

To achieve fast imaging, it is also important to improve the signal-to-noise ratio (SNR) as it decreases with measurement time. The PT signal increases with the pump power, but lower pump power is preferable to avoid photo and/or thermal damage to the sample. Several techniques have been proposed to improve SNR in PT microscopy. As the PT signal is proportional to the change in refractive index, chromophores embedded in liquid crystal, which exhibits a large refractive index change with temperature, produce larger PT signals than those in water [15, 16]. This technique is especially useful for single-molecule absorption spectroscopy. In our previous study, a spatially segmented balanced detection (SBD) method was proposed to improve SNR in forward detection [17]. In SBD, the center and peripheral parts of the transmitted probe beam are separated and detected by a balanced detector. This method was incorporated in the stage scanning PT microscope and improved the PT signal by nearly two times, while also canceling the intensity noise of the probe beam to nearly the shot noise limit.

In this study, we report the development of a fast, high-sensitivity PT microscope by implementing the SBD scheme in a laser scanning microscope. For this purpose, a custom-made bifurcated fiber bundle was incorporated in a laser diode (LD)-based multimodal laser scanning microscope. Simultaneous PT and fluorescence (FL) imaging of gold nanoparticles and FL beads was performed to characterize the performance of the system. 3D visualization of endogenous mouse brain signals was also demonstrated.

2. Experiment

A laser scanning PT microscope equipped with Galvano mirrors was developed based on our LD-based multi-wavelength PT microscope (Fig. 1) [5]. A 405-nm (Nichia NDV4B16) and a 520-nm (Osram PL-520-B1) LDs were used for pumping, with their intensity modulated at different frequencies (f_1 and f_2). The two pump beams were combined using dichroic mirrors and collimated through polarization-maintaining single-mode fiber (PMSMF) and an off axis parabolic mirror (Thorlabs RC08FC-P01) for spatial-mode filtering. A 640-nm LD (Opnext HL63133DG) was used for probing, which was collimated through another PMSMF and a doublet lens. The offset between the pump and probe beams at the focus was controlled by adjusting the position of the doublet lens to reduce the distortion of the PT signal caused by the twin peaks corresponding to the focusing or defocusing of the probe beam [9]. The combined pump and probe beams were directed to an XY Galvano scanner (GSI VM500PLUS) and focused on a sample through an oil immersion objective lens (Olympus PLAPON60X) [numerical aperture (NA) = 1.4]. To acquire images in different focal planes (z-stack), the sample position was controlled in the axial direction using a positioning stage driven by a piezo actuator (MESS-TEK MA-140XLCa).

The SBD method was demonstrated to be useful for high-sensitivity PT imaging in forward detection as it improves signal intensity by nearly two times while also canceling the intensity noise of the probe beam [17]. In PT microscopy, the SNR is usually better in

#259725 Received 19 Feb 2016; revised 24 Mar 2016; accepted 25 Mar 2016; published 5 Apr 2016

forward detection than in backward (epi-)detection [15, 18]. In our previous stage scanning PT microscope, a small mirror was used to separate the center and peripheral parts of the transmitted probe beam. However, it is impractical to incorporate this setup in a laser scanning microscope as it causes complexity in the optical setup. To implement the SBD method in a laser scanning microscope, a custom-made bifurcated fiber bundle with a core fiber size of 50 μm was used to separate the center and peripheral part of the transmitted probe beam. The diameters of the inner and outer circles were 2 and 4 mm, respectively. The incident port of the fiber bundle was placed on a plane conjugate to the pupil of the condenser lens. The center and peripheral parts of the beams separated by the fiber bundle were directed to a balanced photodetector (Newfocus 2307) to cancel the intensity fluctuation of the probe laser. The ratio of the laser powers between the separated two beams depends on the beam spot size at the incident port of the fiber. Thus, the focal lengths of the two lens after the condenser lens were properly selected so that the laser powers of the separated two beams were nearly equal for optimal common mode noise rejection. PT signals (normal mode) at f_1 and f_2 were demodulated by two lock-in amplifiers (Signal recovery 7270). The output from the lock-in amplifiers was recorded by a multichannel date acquisition board (NI PCIe-6321), which was also used to control the Galvano scanner. The time constant of the lock-in amplifier t_c was set at 10 μs and the pixel dwell time was 20 μs. In this case, image acquisition time was about 6 s for 500 x 500 pixels. Modulation frequencies (ω_1 and ω_2) were typically set at 150 kHz and 250 kHz, respectively. We confirmed that the channel interference was negligible as the bandwidth of the lock-in amplifier $1/(2t_c)$ was sufficiently smaller than the difference in modulation frequencies $|f_1 - f_2|$.

A confocal FL detection scheme was also set up for simultaneous PT and FL imaging, in which the FL signal from the sample was detected by a photo-multiplier through a multimode fiber.

To prepare a slice of mouse brain, we fixed adult transgenic mice (two months old, thy1-GFP H-line, Jackson Lab.) by cardiac perfusion with PBS and paraformaldehyde, cut 100-μm slices of the frontal cortex using a vibratome (Leica VT1200), and embedded the slices in UNICRYL resin (Funakoshi). To remove the glycogen, the slices of mouse brain were incubated with 10 mg/ml α-amylase (Tokyo Chemical Industry) in PBS for one hour at 37°C. Then the slices were immunostained with anti-glycogen antibody (a gift from Dr. Otto Baba) to confirm the removal of glycogen. The slices were stained first with the anti-glycogen antibody (12 hours, dilution 1:10 at 4°C), followed by Alexa-Fluor-488 conjugated secondary antibody (Life technologies) staining (2 hours, dilution 1:1000 at 20°C).

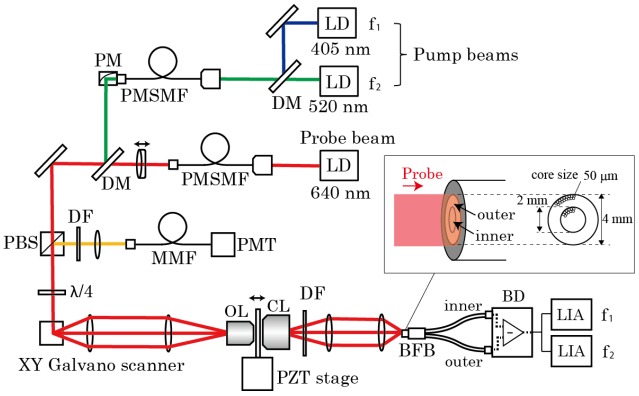

Fig. 1. Schematic illustration of a photothermal microscope equipped with a Galvano scanner and spatially segmented balanced detection. LD: laser diode, PMSMF: polarization-maintaining single-mode fiber, PM: parabolic mirror, DM: dichroic mirror, PBS: polarizing beam splitter, OL: objective lens, CL: condenser lens, DF: dielectric filter, BFB: bifurcated fiber bundle, BD: balanced detector, LIA: lock-in amplifier, MMF: multimode fiber, PMT: photomultiplier tube.

#259725 Received 19 Feb 2016; revised 24 Mar 2016; accepted 25 Mar 2016; published 5 Apr 2016

3. Results and discussion

3.1. Evaluation of the specially segmented balanced detection method

The PT image measured with SBD using the bifurcated fiber bundle was compared with that measured by the conventional detection scheme. Figure 2 shows the PT images of hematoxylin and eosin stained tissue with and without SBD. Here only a 520-nm beam was used for pumping. To obtain a conventional PT image without SBD, the iris diaphragm in the collimator lens was adjusted so that only the center part of the probe beam passed through to maximize the SNR [4, 19], and the transmitted beam was detected using a single photodiode. In contrast, in the SBD, the iris diaphragm of the collimator lens was fully opened and the entire transmitted beam was directed to the incident port of the bifurcated fiber bundle separating the center and peripheral area of the beam. It was confirmed that signal intensity in the SBD was about 1.8 times higher than with conventional detection. Furthermore, the intensity noise of the LD was reduced by 37%. Thus, the SNR was improved by a factor of 4.9. This indicates that image acquisition speed with SBD is 24 times faster than with the conventional scheme to obtain the same SNR using the same pump power, because the SNR is proportional to the square root of the measurement time. In the present setup, imaging speed was limited by the time constant of the lock-in amplifier (10 μs at minimum), which must be lower than the pixel dwell time. However, because the time response of the PT signal is in principle determined by the heat conductivity (~1 MHz at −6 dB point for tightly focused laser beam) [18, 20], it is possible to further decrease the pixel dwell time to a few microseconds by using a fast lock-in amplifier that works with a shorter time constant. To evaluate the effect of light scattering on the lock-in signal, we measured images without pump beam and confirmed that light scattering is negligible (less than 5% of the PT signal).

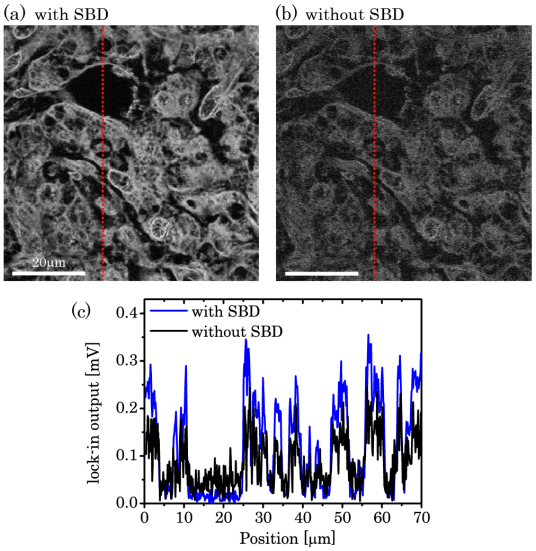

Fig. 2. (a) Phothothermal images of a hematoxylin and eosin stained rabbit ovary (a) with and (b) without spatially segmented balanced detection (SBD). Pump and probe beam power incident on the sample were 8 μW and 4 mW, respectively. Image acquisition time was 6 s at 500 x 500 pixels. (c) Intensity profiles along the vertical lines in (a) (blue) and (b) (black).

3.2. Spatial displacement between photothermal and fluorescence images and spatial resolution

FL imaging is a well-established method for identifying specific biomolecules in a biological specimen, and the combination of PT and FL imaging can provide further information on the tissues because both the nonfluorescent and fluorescent molecules can be visualized at the same time. To characterize the performance of our imaging modality, the spatial displacement

#259725 Received 19 Feb 2016; revised 24 Mar 2016; accepted 25 Mar 2016; published 5 Apr 2016

between the PT and FL images was examined by measuring 1 μm FL beads stained with Nile red [Figs. 3(a)–3(d)]. Here, only the 520-nm beam was used for pumping. PT and FL signals were measured simultaneously during the beam scan. The central position of an individual bead was calculated by fitting them with the Gaussian, from which the magnitude of the displacement between the two images was estimated to be 0.18 μm in the lateral plane. PT and FL images of single bead were acquired by changing the sample position in the axial direction, and the displacement in the axial plane was estimated to be 0.22 μm. These displacements may be caused by misalignment of the confocal pinhole. Since the displacement vector in lateral direction is nearly uniform in the scanning area, it can be corrected by the pixel shift scheme. We confirmed that the signal from the FL beads was a result of the PT effect, as twin peaks appeared in the axial plane when the focal offset of the pump and probe beam was close to zero [9]. The ratio of the signal intensities between FL and PT images are different among individual beads due to a small displacement of image in the axial plane. This is the reason why some of the beads are seemingly presented in one of the imaging modes, though all beads appeared in the FL and PT modes.

The spatial resolution was evaluated by PT imaging of 20 nm gold nanoparticles dispersed in PVA on a glass slide [Figs. 3(e)–3(g)]. The average of the full width at half maximum (FWHM) values for the 61 measured spots was 149 ± 11 nm and 204 ± 10 nm with excitation at 405 nm and 520 nm, respectively. This is slightly larger than the diffraction-limited spot sizes of the pump beams ($0.51\lambda/NA$ = 147 nm and 189 nm for λ = 405 nm and 520 nm). The point spread function (PSF) of PT microscopy is considered to be dependent on the intensity profiles of the pump and probe beams and the refractive index profile at the focal point, and the width of the PSF should be smaller than that of the diffraction-limited spot size of the pump and probe beams [9]. We consider that wavefront distortion induced by optical elements may have caused degradation in the resolution and that further optimization of the optics should provide better resolution. From a stack of images at different focal planes, the FWHM for the axial plane was estimated to be 0.6 μm and 0.7 μm for the 405 nm and 520 nm beams, respectively.

Multi-wavelength PT imaging is invaluable for identifying the molecules observed in the PT image, as the magnitude of the PT signal is proportional to the absorption spectrum [2, 5]. To perform multi-wavelength PT imaging, it is important to investigate the spatial displacement between the images in the different channels, as chromatic aberration of the optical elements may cause distortion of the multi-wavelength images. PT images of gold nanoparticles were obtained simultaneously at the pumping wavelengths of 405 and 520 nm [Figs. 3(e)–3(g)]. The spatial displacement of the image between the two colors was estimated to be smaller than 50 nm in the lateral direction and 0.2 μm in the axial direction, which are about one-third and one-fourth of the PSF width, respectively.

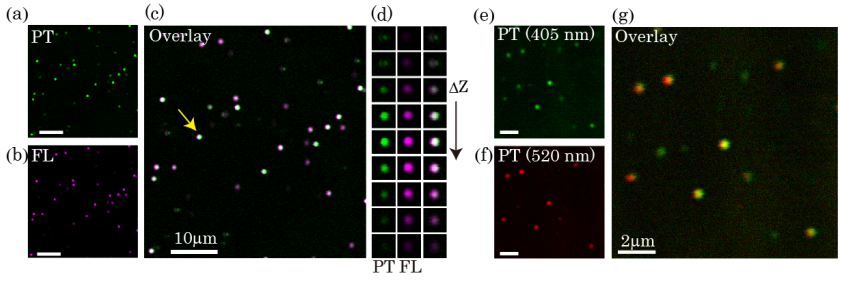

Fig. 3. (a) Phothothermal, (b) fluorescence, and (c) overlay images of 1 μm Nile red beads dispersed in PVA on a glass slide. Pump and probe beam power incident on the sample were 0.5 and 4 mW, respectively. Imaging area was 48 x 48 μm. Scale bars in (a)-(c): 10 μm. (d) Images of a single bead with a different focal plane for the bead designated by the arrow in (c). The step size was 0.27 μm. Simultaneous dual-wavelength photothermal images with excitation at (e) 405 nm and (f) 520 nm, and (c) overlay images. Pump beam power for both was 2 mW and probe beam power was 12 mW. Scale bars in (e)-(g): 2 μm.

#259725 Received 19 Feb 2016; revised 24 Mar 2016; accepted 25 Mar 2016; published 5 Apr 2016

3.3. Imaging of endogenous brain signals

Various linear and nonlinear interactions of light with matter have been applied for label-free brain imaging, such as autofluorescence [21], photoacoustic [11], spontaneous Raman scattering [22, 23], infrared absorption [22, 24], second harmonic generation [21, 25], third harmonic generation (THG) [26], coherent anti-Stokes Raman scattering [27], and stimulated Raman scattering [28]. PT microscopy is a powerful tool for visualizing endogenous signals in biological tissue, yet little brain imaging has been reported. We performed simultaneous PT and FL imaging of a fixed slice of transgenic mouse brain expressing yellow fluorescent protein (YFP). Figure 4 shows the results of simultaneous PT and confocal FL imaging of different layers of the mouse brain cortex. FL images visualize neurons expressing YFP at the dendrite terminals [Fig. 4(a)], a dendrite [Fig. 4(b)], and cell bodies [Fig. 4(c)], respectively. The PT images show distinct structures and organization. Red blood cells and vessels can be identified morphologically. They produce strong PT signals as they may contain heme proteins [Figs. 4(a) and 4(b)]. A Y-shaped junction of a vessel is also observed in Fig. 4(b). Although cardiac perfusion with PBS is conducted in the sample preparation, there is a possibility that red blood cells are fragmented or stacked in a vessel and result in the PT signal of a vessel.

The cell bodies of the neurons appear as dark shadows. It should be noted that fine structures are observed in all areas of the brain cortex. Figures 5(a) and 5(b) shows close-up images around an axon and the dendrites of neurons. Bright specks with diameters of around 1 μm appear surrounding the cell bodies. These are attributable to the lipofuscins in lysosomes as weak autofluorescence is detected [21]. Sponge-like structures of sub-micrometer size cover large areas of the tissue. The combined PT and FL images show that the axon and dendrites visualized in the FL image do not overlap with the fine structures in the PT images. This indicates that the contrasting agent of the sponge-like structure is outside the neuron. A stack of images in discrete z-steps [Visualization 1] clearly shows the depth profile of the shadow contrast of the cell bodies and the fine structures. The 3D-imaging capability is also demonstrated [Fig. 5(c)] by the reconstructed 3D model of a volume scan.

To obtain further information on the fine structures observed in the PT image, simultaneous dual-wavelength imaging was performed using two pump beams at wavelengths of 405 and 520 nm [Fig. 5(d)]. From the dual-wavelength PT imaging of the sponge structures, the absorbance ratio between 520 and 405 nm is calculated to be about 0.3. The brain slice shows a faint yellow color. Thus, the light absorption of the brain tissue is predominantly attributed to the species contained in the sponge structures. In contrast, the intensity ratio of the bright specks around the dark shadows is ~0.7, which suggests that the bright specks and the sponge structures are composed of different species. To exclude the possibility that transgenic expression of YFP affects the PT signal, we acquired PT images of a wild type mouse brain and found identical fine sponge structures. This indicates that the PT signal originates mainly from the endogenous chromophores in the brain.

We presume that the fine sponge-like structures can be attributed to the lipids comprising 30-60% of the brain. Hydrophobic dyes such as lutein and zeaxanthin that can cross the blood-brain barrier and/or lipid peroxides may serve as PT contrast agents. Lutein and zeaxanthin are carotenoid contained in grain, which are concentrated in the neural retina and brain neocortex [29, 30]. It is suggested that lipid has a steeper refractive index/temperature slope (~1 x 10^{-3} K^{-1}) [31], and thus the chromophores in the lipids result in a significant PT signal. It is interesting to note that the PT image of the brain cortex is similar to the THG image [26]. Lipid bodies are a major source of contrast in THG microscopy, which is used to visualize lipid structures in the brain. Interestingly, however, unlike the THG signal, PT signal was not seen in neurons and myelin sheaths, but rather found in intracellular organelles of non-neuronal cells (Fig. 5). In this regards, in THG imaging, a partial phase match of third-order susceptibility at the focal produces the TH signal and the signal is most intense when a structure is half the size of the focal volume. This can result in the signal intensity distribution different from the concentration distribution and may work as a kind of spatial filtering

#259725 Received 19 Feb 2016; revised 24 Mar 2016; accepted 25 Mar 2016; published 5 Apr 2016

function to coarse grain the distribution reducing the intensity of finer structure. This may be the reason why THG imaging provides more uniform distribution than PT method [26]. On the other hand, since the contrast mechanisms are different between the THG and PT images, they may provide complemental information on the structure or composition of the lipid.

We also evaluated the possibility that the fine sponge-like structures represent glycogen granules, which is abundant in astrocytes. However, the PT signal did not change after treatment with amylase, which digests glycogen in the sample. Moreover, the PT signals rarely overlapped with glycogen immune-reactive granules.

Previous study showed that the PT signal of live cultured neurons originated from cytochrome c [32]. Cytochrome c is water solvable and refractive index/temperature slope of water is 1 x 10^{-4} K^{-1}, while lipid has a steeper slope [31]. Therefore, the PT signal of lipid should be larger that of cytochrome c in imaging of brain slice even though they may have comparable optical absorption. However, there is still a possibility that cytochrome c contributes to the PT signal and careful study is need to this point.

Lipid metabolism in the brain is closely related to neurodegeneration illnesses such as Alzheimer's disease [24, 33]. Hence, the ability to image both the neuron and the lipid structure at high spatial resolution will be a powerful technique for the study of such diseases.

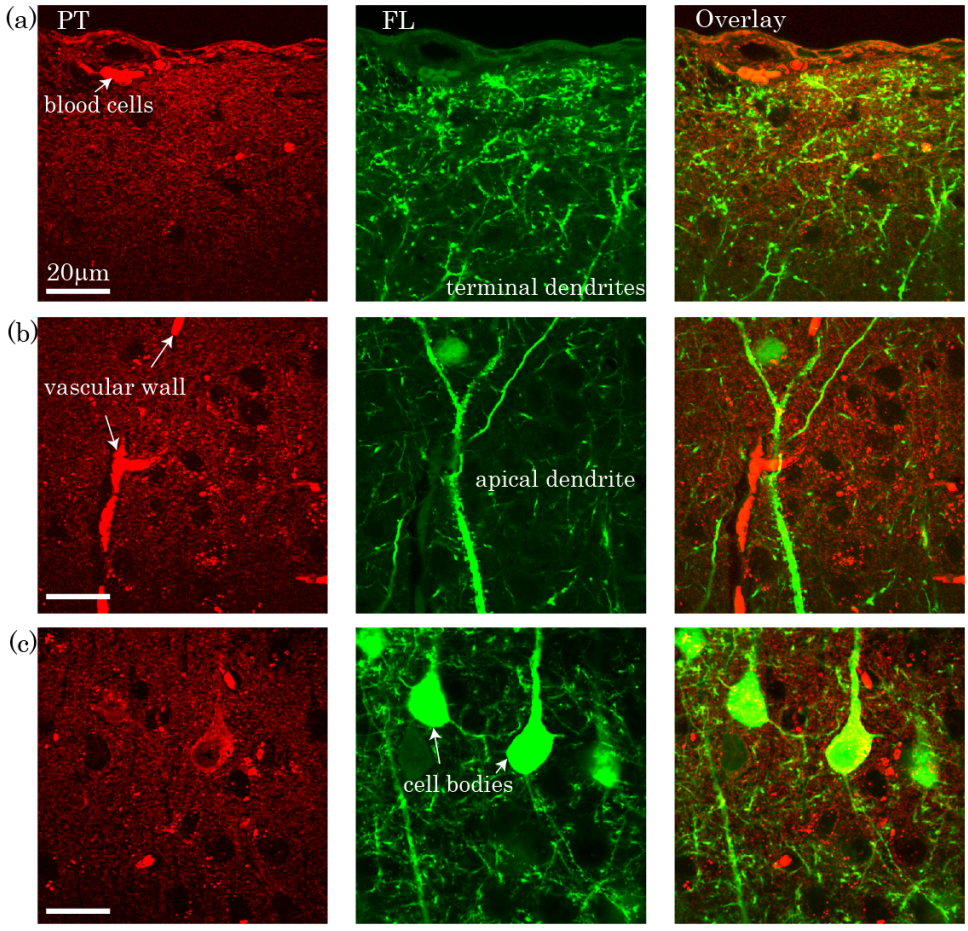

Fig. 4. Simultaneous photothermal (PT) and fluorescence (FL) imaging of mouse brain cortex at (a) the surface, (b) layer II/III, and (c) layer IV. Left and center panels show the PT and FL images, respectively, and their overlay is shown in the right panel. The pump and probe beam power incident on the sample were 0.5 and 4 mW, respectively. Image acquisition time was 6 s at 500 x 500 pixels.

#259725 Received 19 Feb 2016; revised 24 Mar 2016; accepted 25 Mar 2016; published 5 Apr 2016

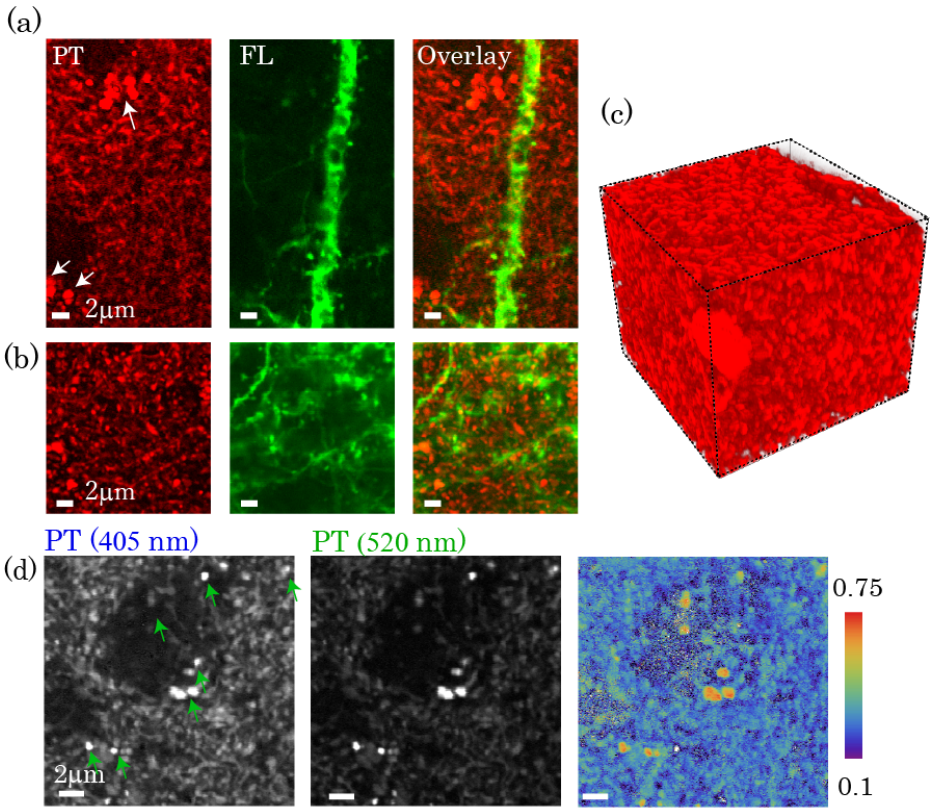

Fig. 5. Close-up photothermal (PT) and fluorescence (FL) images of mouse brain cortex. PT and FL images around (a) a dendrite and (b) axons. Arrows shows bright specks localized around cell bodies, which are attributable to lipofuscins in lysosomes. (c) Reconstructed 3D model of PT signal in cortex. Image size is 23 x 23 x 21 μm with 400 x 400 x 80 voxels and acquisition time was about 9 minutes. A stack of 30 images of brain cortex was acquired by changing the sample position in the axial direction with a step size of 0.68 μm (see Visualization 1). Each image size is 70 x 70 μm with 600 x 600 pixels. Acquisition times were 5 minutes (d) dual-wavelength PT images around a cell body with excitation at 405 nm (left) and 520 nm (center), and their ratio image (right).

4. Conclusion

Fast, high-sensitivity PT microscopic imaging was conducted by incorporating the SBD scheme into a laser scanning multi-wavelength and multimodal microscope. It was confirmed that SNR improves by a factor of 4.9; thus image acquisition time becomes 24 times faster than that of conventional detection with the same SNR and pump power. Simultaneous PT and confocal FL imaging of transgenic mouse brain tissue expressing YFP was demonstrated. The PT method detected endogenous non-fluorescent chromophores in brain tissue and various organizations such as blood cells, lipofuscin in lysosomes, and fine sponge structures, which are presumably attributable to lipids, all visualized with high 3D resolution. As this imaging modality is based on compact, low-cost laser diodes, it will be widely useful in the life and medical sciences, e.g., for lipid metabolism in the brain and related neurodegenerative diseases.

Acknowledgments

This study was financially supported by a Grant-in-Aid for Scientific Research (No. 15K17735) received from the Japan Society for the Promotion of Science.

#259725 Received 19 Feb 2016; revised 24 Mar 2016; accepted 25 Mar 2016; published 5 Apr 2016